Received: 28 December 2016 | Revised: 20 June 2017 | Accepted: 26 October 2017

DOI: 10.1002/nag.2761

RESEARCH ARTICLE

WILEY

Implementation of a coupled plastic damage distinct lattice spring model for dynamic crack propagation in geomaterials

Chao Jiang[1,2] | Gao-Feng Zhao[1]

[1]State Key Laboratory of Hydraulic Engineering Simulation and Safety, School of Civil Engineering, Tianjin University, Tianjin 300350, China

[2]School of Civil and Environmental Engineering, The University of New South Wales, Sydney, NSW 2052, Australia

Correspondence
Gao-Feng Zhao, State Key Laboratory of Hydraulic Engineering Simulation and Safety, School of Civil Engineering, Tianjin University, Tianjin 300350, China.
Email: gaofeng.zhao@tju.edu.cn

Summary

This paper studies dynamic crack propagation by employing the distinct lattice spring model (DLSM) and 3-dimensional (3D) printing technique. A damage-plasticity model was developed and implemented in a 2D DLSM. Applicability of the damage-plasticity DLSM was verified against analytical elastic solutions and experimental results for crack propagation. As a physical analogy, dynamic fracturing tests were conducted on 3D printed specimens using the split Hopkinson pressure bar. The dynamic stress intensity factors were recorded, and crack paths were captured by a high-speed camera. A parametric study was conducted to find the influences of the parameters on cracking behaviors, including initial and peak fracture toughness, crack speed, and crack patterns. Finally, selection of parameters for the damage-plasticity model was determined through the comparison of numerical predictions and the experimentally observed cracking features.

KEYWORDS

3D printing, crack propagation, damage-plasticity model, lattice spring model

1 | INTRODUCTION

Understanding crack propagation in geo-materials is important for engineering practices. Complicated geological mediums usually contain flaws and become unpredictable. Numerical methods can provide insights into the mechanism of the crack propagation, and they have been used extensively in the study of rock dynamics due to the development of computer technology. However, many numerical simulations of crack failures merely focus on the morphology rather than both the qualitative and quantitative modeling of the entire fracture behavior. For example, Lee and Jeon[1] used a discrete element method (DEM)-based simulator, *particle flow code*, for crack coalescence on granite, obtaining similar crack patterns but a mismatch on the crack initiation, coalescence, and peak stresses. Haeri et al[2] and Haeri et al[3] used the boundary element method to obtain the satisfied crack path, but other crack features, including stress or crack speed, were not mentioned. Similarly, Dai et al[4] used the scaled boundary finite element method (SBFEM) to predict the final crack path, disregarding the features in the evolution process. Ayatollahi et al[5] used the FEM-based simulator *Abaqus* to simulate the crack path in semi-circular bending specimens as well as the fracture toughness, but it can only be applied on simple geometry of the model with single fracture. Moreover, most of the aforementioned crack simulations were conducted under static loading. In dynamic crack propagation, where scenarios are more complicated, the crack features are associated with the loading conditions and become unpredictable. Therefore, a proper model should be developed with the help of an experiment using both qualitative and quantitative validations.

In dynamic crack propagation, the crack speed is an important characteristic because it is associated with the mechanical behavior of the material. For example, the increasing crack speed will either increase or decrease the fracture toughness of polymers.[6] Zhang and Zhao[7] summarized a series of data among the tests on rock from the literature and stated that most of the ratios of maximum crack velocity to Rayleigh wave speed are in the range of 0.2 to 0.71, which depends on the material and loading conditions. Bhat et al[8] incorporated the crack speed into the constitutive model to form a rate-dependent model. Many rate-dependent models were proposed as a trend in dynamic fracturing, but validations of the crack speed are few in number. Therefore, a model considering all the crack features, including the significant crack speed, is essential.

It is widely accepted that discontinuum-based models are advantageous over continuum-based models for rock fracturing problems, especially in complex geometries due to their discrete nature and the simple mathematic treatment in the micro constitutive models among the interacting elements.[9] The most popular discontinuum-based methods are DEMs.[10] However, the high computational cost limits their applications and the accuracy of the results. The distinct lattice spring model (DLSM)[11] was originally developed in 3 dimensions. As a newly developed method, it improves the efficiency of computation by reducing the number of degrees of freedom and eliminates the limitation on Poisson's ratios compared with the conventional DEM. Its quasi-static validations on the elastic region of the material can be found in Zhao[11] and Zhao et al.[12] In addition, dynamic problems, such as wave propagation through jointed rock mass,[13] failure in jointed rock mass,[14] dynamic crack propagation,[15,16] and soil desiccation cracking,[17] have been demonstrated extensively in the aforementioned papers. However, the study of complicated problems by DLSM is limited due to 2 barriers. The first one is the computational ability. Although further development of DLSM via a parallel algorithm on GPU makes it possible to achieve a speedup of 23,[18] it is still a problem to conduct a substantial amount of calculation (eg, for parametric study in engineering scales). In addition, high-performance computers are expensive and not feasible for all researchers. To reduce the burden on the calculation, a 2D version of DLSM was derived, which can also dramatically enhance the resolution with the same number of particles in 3D. A triangular 2D DLSM model was demonstrated in Zhao[11] and Zhao et al.[19] Zhao[20] further extended the 2D model to the large deformation of the structures. The second barrier is on the constitutive model. Like the conventional DEMs, the basic micro components linking the elements in DLSM are the normal stiffness and shear stiffness. The original DLSM adopts the simplest elasto-brittle constitutive models for both normal and shear stiffness, and the effects on simulating brittle fracture seem satisfied by qualitative comparison of the failure patterns (eg, Zhao[14]). With quantitative analysis, Kazerani et al[15] and Zhao et al[21] used rate-dependent cohesive models in DLSM for dynamic crack propagation in PMMA and uniaxial tensile strength of sandstone. Although the crack speed and energy dissipation were simulated, their constitutive models require tedious calibration of the parameters. Moreover, their models do not consider plasticity of the material, which limits their applications where non-linear mechanical behaviors are present. Therefore, a constitutive model in a simple form incorporating both damage and plasticity modeling is in demand.

The aim of this paper is to develop a simple constitutive model for DLSM that accounts for the fracture toughness, crack speed, and crack pattern. The constitutive model will be implemented in a 2D DLSM and examined with dynamic fracturing tests on 3D printed specimens. The context is organized as follows. A 2D DLSM model is introduced, and the proposed coupled damage-plasticity constitutive model is implemented, which is later validated against analytical solutions in the elastic domain and experimental fracture patterns. Then, the split Hopkinson pressure bar (SHPB) test on 3D printed specimens is described, in which the experimental data were referenced for parametric study of the new model. A series of parametric studies are conducted under the scope of macro crack features, including initial/peak fracture toughness, crack speed, and crack patterns. In addition, particle size effects are investigated. After that, a simplified constitutive model is proposed for the simulation of our experiment based on the previous parametric study. Lastly, the procedures for parameter selection for our experiment are illustrated.

2 | TWO-DIMENSIONAL DISTINCT LATTICE SPRING MODEL

2.1 | Distinct lattice spring model lattice and calculation scheme

The DLSM was proposed by Zhao[11] as an intrinsic 3D model. In the 2D version of DLSM presented in this paper, the particles are aligned in a regular lattice pattern. Two lattice types are presented, ie, type A and type B (refer to Figure 1). In lattice type A, the diagonal linkages only exist in every 2 particles in each direction, while every particle has diagonal linkages in type B. The crossed diagonal linkages in type B are not actually intersecting and are independent in the calculations. Every linkage consists of a pair of springs, namely, a normal spring and a shear spring,

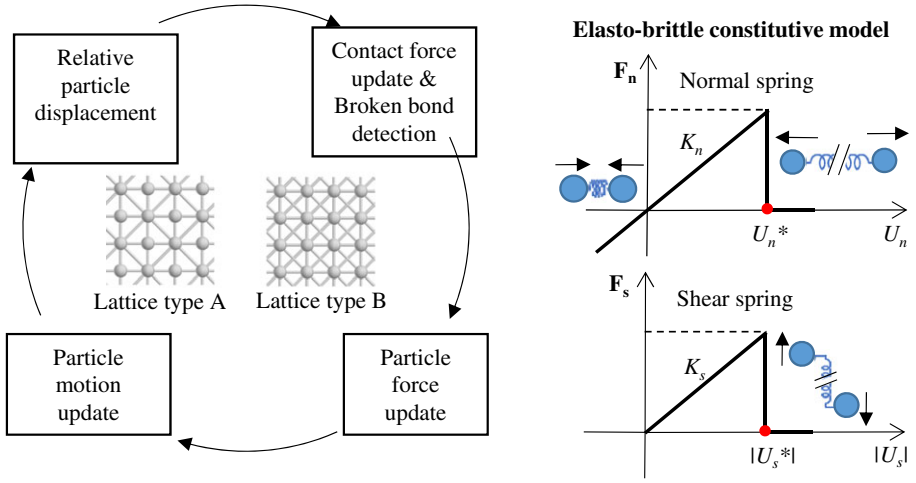

FIGURE 1 The lattice types, calculation cycle, and elasto-brittle constitutive model in DLSM [Colour figure can be viewed at wileyonlinelibrary.com]

connecting the particles with prescribed sizes. In 3D DLSM, the simple elasto-brittle model was used, and it can be ported to the 2D version as well. Either spring has its critical displacement (U_n^* or U_s^*) within which the spring obeys Hooke's law and beyond which the particles will only have a contact bond with zero strength. The breakage of either spring will cause the pair of springs to disappear. The implementation is very similar to the 3D model, except the absence of the third dimension in the calculations. The details of the equations of 3D DLSM can be found in Zhao et al,[12] and only a brief introduction on any differences from 3D DLSM will be presented.

The calculation cycle of DLSM is also shown in Figure 1. When the relative particle displacement is obtained initially or from the last time step, the contact bonds between the particles with a specific constitutive law can be used to calculate the new contact force and detect any breakage. Obeying Hooke's law, the normal force and shear force between the 2 particles are given as

$$F_n^{ij} = k_n U_n^{ij} \tag{1}$$

and

$$F_s^{ij} = k_s U_s^{ij} \tag{2}$$

where k_n or k_s is the stiffness of the spring, U_n^{ij} is the relative displacement between 2 particles i and j, and U_s^{ij} is the relative shear deformation calculated using a local strain method from a particle cluster rather than the shear displacement of the 2 particles,[12] which makes DLSM distinct from classical LSMs by removal of the limitation on various Poisson's ratios. The shear deformation is calculated as[12]

$$U_n^{ij} = [\varepsilon]_{bond} \cdot \mathbf{n} l - \left(\left([\varepsilon]_{bond} \cdot \mathbf{n} l \right) \cdot \mathbf{n} \right) \mathbf{n} \tag{3}$$

where l is the initial bond length, $[\varepsilon]_{bond}$ is the bond local strain, which is evaluated as the average of the 2 linked particles, and $\mathbf{n}$ is the normal vector of the spring. This approach also causes the model to be rotational invariant. More details can be found in Zhao et al.[12] All the contact forces linking the particle are summed so that the total forces on the particles are updated. By Newton's second law, the particle accelerations are known, and the particle velocities are obtained as

$$\dot{U}^{(t+\Delta t/2)} = \dot{U}^{(t-\Delta t/2)} + \ddot{U} \Delta t \tag{4}$$

where Δt is the time step, $\dot{U}^{(t+\Delta t/2)}$ is the particle velocity at $t + \Delta t/2$, $\dot{U}^{(t-\Delta t/2)}$ is the particle velocity at $t - \Delta t/2$, and $\ddot{U}$ is the acceleration. Lastly, the new displacements of particles are calculated as

$$U^{(t+\Delta t)} = U^{(t)} + \dot{U}^{(t+\Delta t/2)} \Delta t \tag{5}$$

where $U^{(t+\Delta t)}$ is the displacement at the next time step, and $U^{(t)}$ is the displacement at t.

The other difference in the 2D model compared with the 3D model are forms of the formulas of the spring stiffness (k_n and k_s), which are still based on macro material properties (Young's modulus E and Poisson's ratio v) and derived by Cauchy-Born rules and the hyperelasticity theory. The equations[19] for k_n and k_s in the elastic domain for the plane stress condition are

$$k_n = \frac{2E}{\alpha^{2D}(1-v)} \tag{6}$$

$$k_s = \frac{2(1-3v)E}{\alpha^{2D}(1-v^2)}. \tag{7}$$

In the plane strain condition, they are

$$k_n = \frac{2E}{\alpha^{2D}(1+v)(1-2v)} \tag{8}$$

$$k_s = \frac{3(1-4v)E}{\alpha^{2D}(1+v)(1-2v)} \tag{9}$$

where α^{2D} can be estimated as

$$\alpha^{2D} = \frac{\sum l_i^2}{A\Delta} \tag{10}$$

where l_i is the original length of the i^{th} spring, A is the area of the represented geometry model, and Δ is the unit thickness in the third dimension.

2.2 | Coupled damage-plasticity constitutive model

The scope of this paper covers the crack propagation dominated from Mode-I micro failure, so we forbid the breakage of the shear springs on purpose by ensuring that the shear springs are within the elastic portion of the constitutive law. Therefore, the interactions by the shear springs have no difference from an elasto-brittle model or a cohesive model. It is noted that the breakage of the normal spring will induce the breakage of the associated shear spring simultaneously, and thus a stress-free crack is ensured. In this paper, a coupled damage-plasticity constitutive model is proposed and implemented into the 2D DLSM for the normal spring only. The extension for the shear spring is straightforward. The proposed constitutive law for the normal spring is plotted in Figure 2. It is a trilinear model that couples the damage (refer to Figure 2A) and plasticity behavior (refer to Figure 2B) during unloading, and the form of the constitutive model is governed by 4 parameters (ie, β, γ, U_n^*, and λ_{dp}). The geometric ratios β and γ are indicated in Figure 2C. It is noted that a special bilinear constitutive form can be derived from the trilinear model with $\gamma = 0.5$, as shown in Figure 2D. λ_{dp} is the damage-plasticity weight ($0 \le \lambda_{dp} \le 1$), which is introduced to couple the damage and plasticity components with the equation expressed as

$$F_n^c = (\lambda_{dp})F_n^d + (1-\lambda_{dp})F_n^p \tag{11}$$

where F_n^c is the coupled normal force in the springs, F_n^d is the normal force component of the damage model, and F_n^p is the normal force component of the plasticity model. The normal force component of the damage model F_n^d can be expressed as

$$F_n^d = k_d U_n \tag{12}$$

where $k_d$is the slope of unloading/reloading in the damage model, which is

$$k_d = \begin{cases} k_n & ; \quad u_n^h \le \beta U_n^* \\ k_n \dfrac{\beta}{u_n^h}\left[U_n^* - \dfrac{(\gamma-1)}{\gamma(\beta-1)}(u_n^h - \beta U_n^*)\right] & ; \quad \beta U_n^* \le u_n^h \le (\gamma+\beta-\gamma\beta)U_n^* \\ k_n\gamma\beta\left[\dfrac{U_n^*}{u_n^h} + \dfrac{u_n^h - (\gamma+\beta-\gamma\beta)U_n^*}{u_n^h(\gamma+\beta-\gamma\beta-1)}\right] & ; \quad (\gamma+\beta-\gamma\beta)U_n^* \le u_n^h \le U_n^* \\ 0 & ; \quad u_n^h \le U_n^* \end{cases} \tag{13}$$

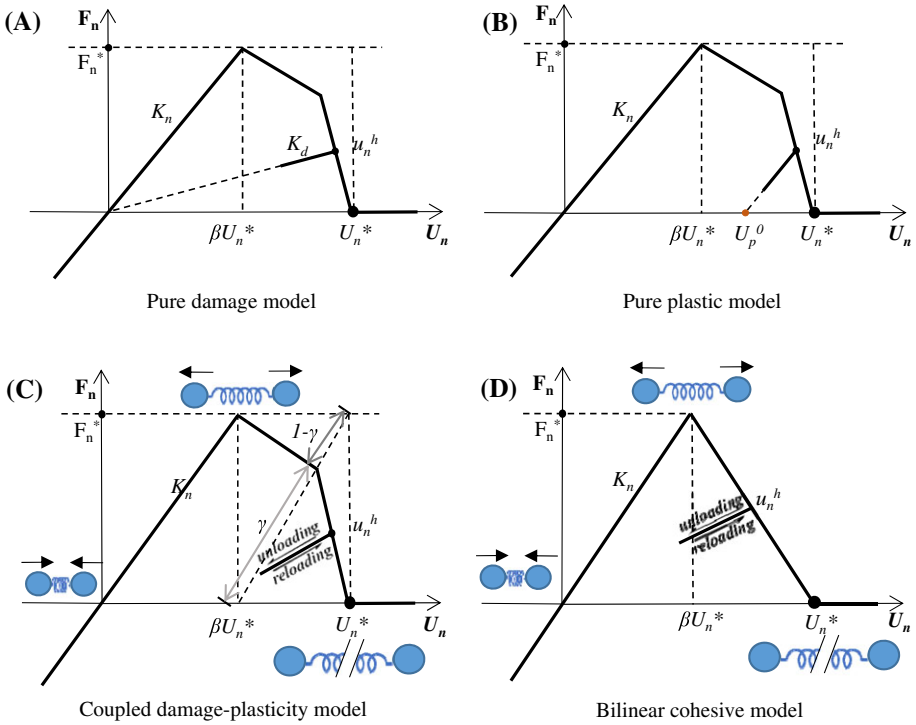

FIGURE 2 The constitutive models in 2D DLSM. (A) Pure damaged model. (B) Pure plastic model. (C) Coupled damage-plasticity model. (D) A special case for the proposed model: bilinear cohesive model [Colour figure can be viewed at wileyonlinelibrary.com]

where k_n is the initial normal spring stiffness and u_n^h is the historical maximum deformation in the springs. The normal force component of the plasticity model F_n^p can be expressed as

$$F_n^p = k_n\left(U_n - U_p^0\right) \tag{14}$$

where U_p^0 corresponds to the displacement on the unloading curve at $F_n^p = 0$, and the equations are

$$U_p^0 = \begin{cases} 0 & ; \quad u_n^h \le \beta U_n^* \\ \beta U_n^*\left(1-\dfrac{k_d}{k_n}\right) & ; \quad \beta U_n^* \le u_n^h \le (\gamma+\beta-\gamma\beta)U_n^* \\ U_n^*\left(1-\dfrac{k_d}{k_n}\right) & ; \quad (\gamma+\beta-\gamma\beta)U_n^* \le u_n^h \le U_n^* \\ U_n & ; \quad u_n^h \ge U_n^* \end{cases}. \tag{15}$$

2.3 | Validation

2.3.1 | Validations of the elastic region of the model

In the beginning, validations are conducted within the elastic region of the model under quasi-static loading. The first scenario is a model with a size of 100 mm × 100 mm subjected to 10 MPa of tension on the top (refer to Figure 3A). The displacement on the top surface is calculated according to various Poisson's ratios, and the result for lattice type A is presented in the graph. Actually, both lattice type A and type B are under examination, and the percentage errors for both are summarized in Table 1. It is noted that the error in lattice type B is unacceptable for large Poisson's ratios, and it even causes numerical instability when v approaches 0.4. In comparison, the error is quite reasonable for lattice type A, and the agreement with the FEM results covers a large range of Poisson's ratios. The range can cover most of the materials, at least for all the isotropic rocks whose values fall in the range from 0.05 to 0.45.[22] It is also noted that a Poisson's ratio of 0.5 is numerically unfeasible in a plain strain condition according to Equations 8 and 9. From the

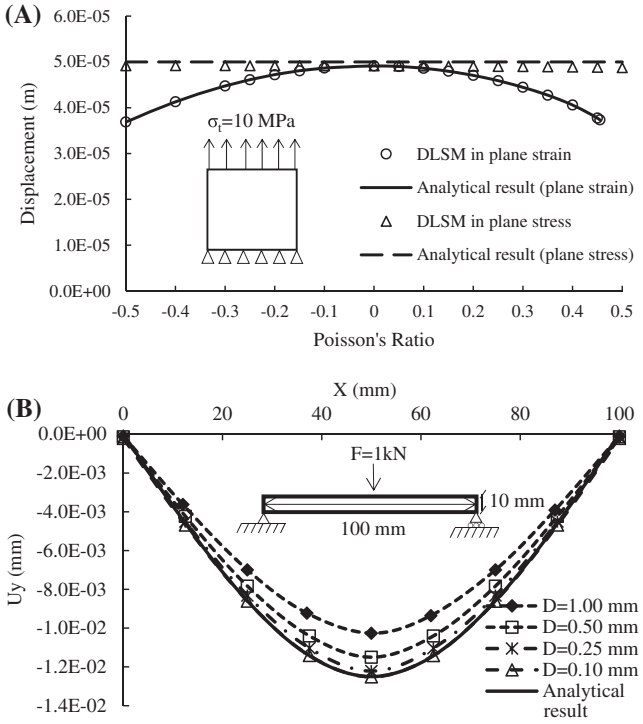

FIGURE 3 Validations for elastic region of the model. (A) Comparison of the displacement of the top surface with different Poisson's ratio. (B) Deflection of the span according to different particle sizes

TABLE 1 Percentage error compared with the analytical solution with different Poisson's ratios

Lattice	Plain Stress		Plain Stress	
Error υ	Type A		Type B	
−0.5	−1.7	−6.4	−1.7	−6.6
−0.4	−1.6	−6.6	−1.6	−6.4
−0.3	−1.6	−6.5	−1.6	−6.1
−0.2	−1.7	−5.8	−1.7	−5.5
−0.1	−1.7	−4.4	−1.7	−4.3
0	−1.7	−4.4	−1.7	−2.0
0.05	−1.8	−0.1	−1.8	0.0
0.1	−1.8	2.3	−1.8	2.9
0.2	−1.9	9.6	−2.0	15.3
0.3	−2.0	23.1	−2.3	66.2
0.4	−2.2	51.6	−3.3	Instable
0.45	−2.3	80.9	−5.3	Instable
0.5	−2.5	139.6	N/A	N/A

above simulations, it is proven that lattice type A is stable for various Poisson's ratios and that lattice type B should be disregarded. For the rest of the paper, only lattice type A is considered.

The second validation example is the simply supported beam subjected to a central point load of 1 kN (refer to Figure 3B). The span is 100 mm in length and 10 mm in depth. The deformations on the beam are plotted with particle sizes of 1 mm, 0.5 m, 0.25 mm, and 0.1 mm. The results indicate that, with enough decrease in the particle size, DLSM approaches the analytical solution.

The 2 examples above have shown the accuracy and stability of this 2D version of DLSM by lattice type A for quasi-static simulations.

2.3.2 | Validations of crack propagation patterns

Two more validations of crack propagation are illustrated. The purpose is to illustrate that the proposed model is stable in reproducing a wide range of cracking phenomena, including wing cracks and crack coalescence.

A rectangular sample of 20 mm × 40 mm is generated. A line crack is inserted in the center of the rectangle with an inclination angle. A compressive stress is applied from the top surface. As seen in Figure 4, DLSM with the proposed model can reproduce a similar crack path as in the experiment on resin from Nemat-Nasser and Horii.[23] In DLSM, only tensile and shear springs are incorporated. However, Wang and Mora[24] conducted the simulation on the same geometry (refer to Figure 4C) and concluded that the correct path cannot be reproduced without considering particle rotation in their Lattice Solid Model, which resulted in the situation that the cracks "grow slowly and discontinuously, and several *en echelon* cracks appear".[24] The correct path can only be reproduced when normal, shear stiffness, bending stiffness, and single particle rotation are all included in their models. In comparison, our simple 2-spring controlled DLSM works quite effectively.

The second example simulates crack propagation on a perforated epoxy plate by tensile stress on the top surface. Following Al-Ostaz and Jasiuk,[25] the input material properties of the model are as follows: $E = 3.26$ GPa, $\upsilon = 0.38$, and $\rho = 1.1$ g/cm^3. Different constitutive models are adopted for the simulation. Not much difference is noticed with different cohesive models from Figure 5B to E. Their tiny differences occur at the coalescence within the 2 holes marked in the figures. It is emphasized that there are negligible differences in the general crack pattern even in the purely plastic constitutive model in Figure 5C. The last one shown in Figure 5F is the result with the elasto-brittle constitutive model, which shows a different crack path. However, compared with the experimental result in Figure 5A, it seems more proper to simulate this piece of epoxy via cohesive models.

3 | EXPERIMENT

The purpose of the experiment designed here is to provide a benchmark on crack propagation. A homogeneous material is required to eliminate the influence from material heterogeneity. Hence, a highly homogeneous 3D printing material is used in this study.

3.1 | Sample preparation

The material and the sample preparation method in this paper are the same as those in Jiang et al.[26] The printer is *Projet660* from 3D system Inc. The material used is called *VisiJet PXLCore*, and its main composite is calcium sulfate hemihydrate $CaSO_4.0.5H_2O$. It is an extremely fine material with a particle size of approximately 50 μm by our measurement under an optical microscope (refer to Figure 6A). The cracked straight-through Brazilian disc (CSTBD) model is used for

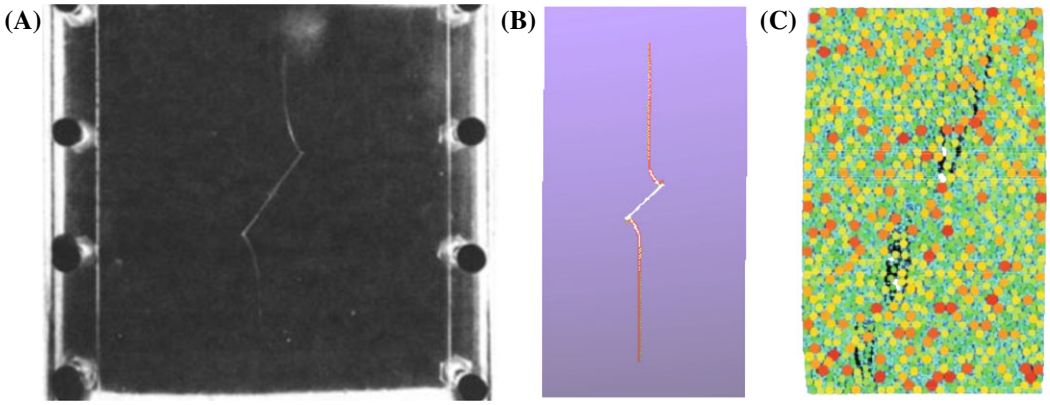

FIGURE 4 Comparison of wing cracks under compression. (A) Experimental results on resin from Nemat-Nasser and Horii.[23] (B) DLSM simulation. (C) LSM simulation without particle rotation from Wang and Mora[24] [Colour figure can be viewed at wileyonlinelibrary.com]

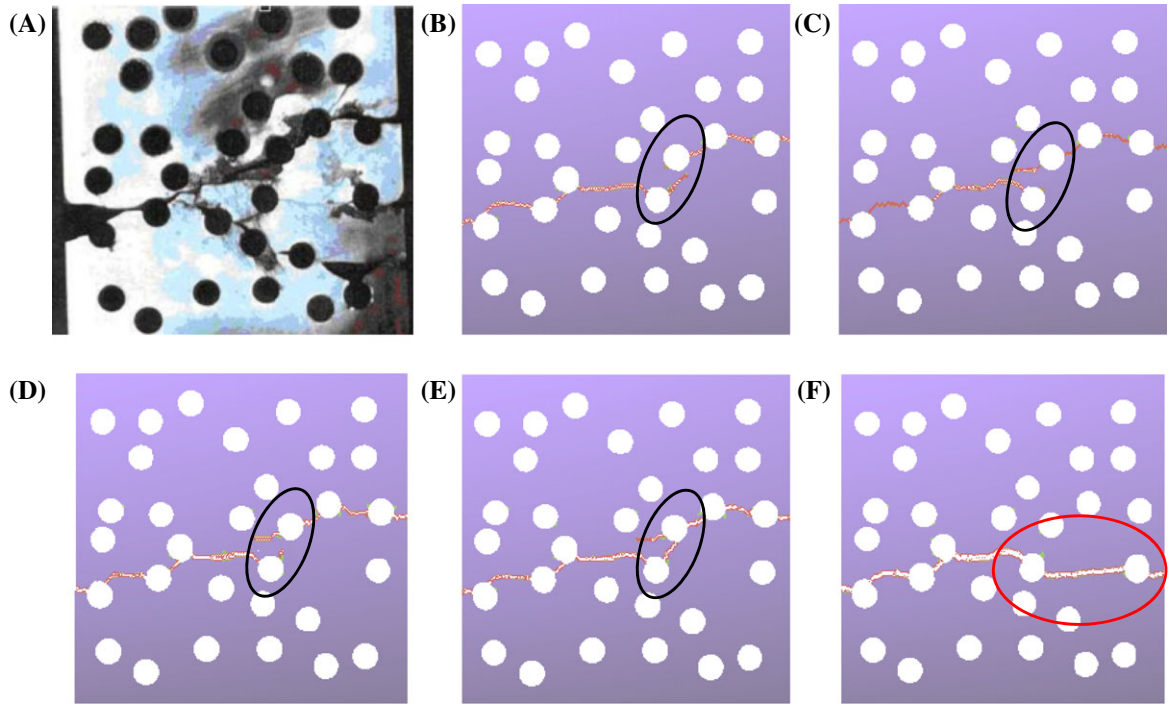

FIGURE 5 Crack path on an epoxy sheet in (A) the experiment from Al-Ostaz and Jasiuk[25], and DLSM with (B) $\beta = 0.3$; $\lambda_{dp} = 1$; $\gamma = 0.5$ (C) $\beta = 0.3$; $\lambda_{dp} = 0$; $\gamma = 0.5$ (D) $\beta = 0.5$; $\lambda_{dp} = 1$; $\gamma = 0.5$ (E) $\beta = 0.7$; $\lambda_{dp} = 1$; $\gamma = 0.5$ (F) elasto-brittle constitutive model [Colour figure can be viewed at wileyonlinelibrary.com]

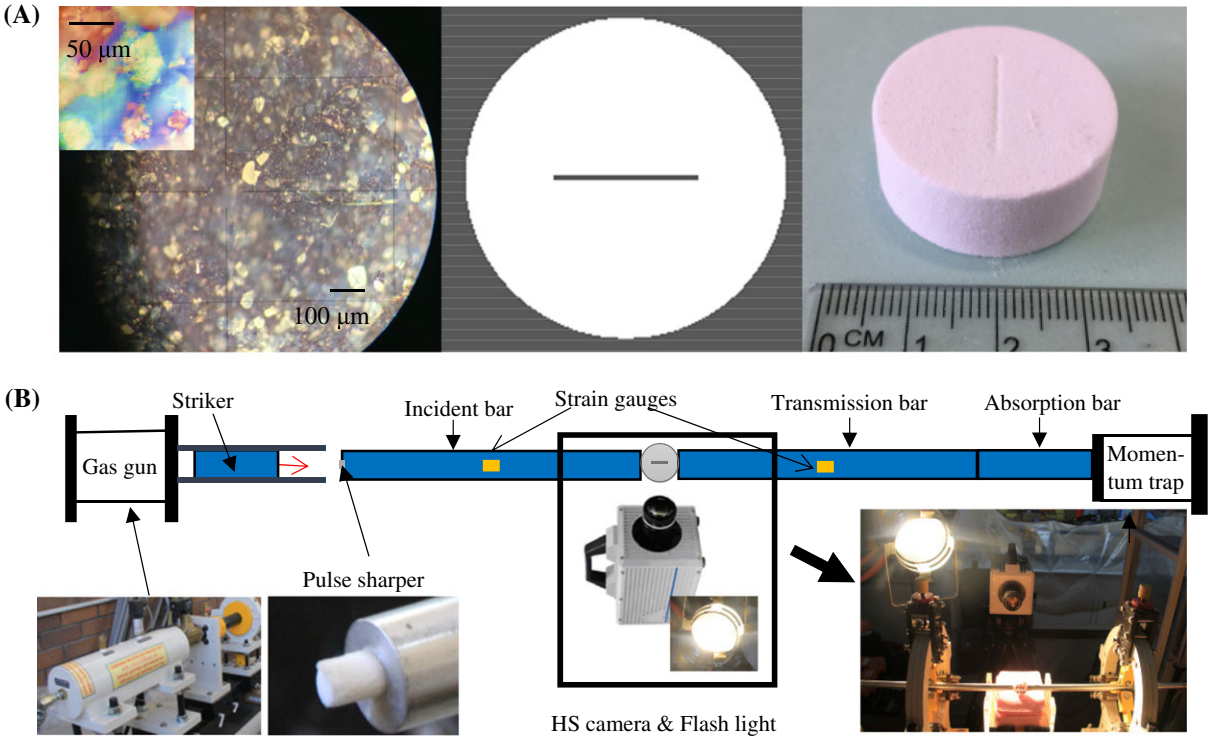

FIGURE 6 (A) The particles under microscopy from the 3D printed material, specimen geometry, and the photo of a specimen. (B) SHPB setup of the dynamic fracturing tests [Colour figure can be viewed at wileyonlinelibrary.com]

evaluation of the dynamic fracture toughness of this material. The diameter of the disc is 30 mm, and the thickness is 12 mm. The length of the straight-through notch is 13.5 mm, and the notch width is 0.5 mm. It is noted that the notch was designed as a hollow section, but the powder still fills the notch during the printing. The powder did not make

contact with the binder, so the strength provided from the unbounded powder is negligible. The unbounded state of the powder can be observed with CT scanning, which was described in Jiang et al.[26] The equation for calculation of the static fracture toughness[27] is

$$K_{IC}\frac{P_{cr}}{\sqrt{Rt}}Y \tag{16}$$

where P_{cr} is the critical force, R is the radius of the disc, and t is the thickness. Y is the geometrical dimensionless factor, and it is 0.5 for our geometry.[27] We assume that this equation is applicable to our dynamic situation if the stress equilibrium is achieved in the tests, and thus the dynamic stress intensity factor is calculated in that manner.

3.2 | Split Hopkinson pressure bar system

The dynamic fracturing on the 3D printed specimens is accomplished by the SHPB system, which is able to achieve high loading rates. The SHPB system consists of a pressure control station, a gas gun, a striker, an incident bar, a transmitted bar, an absorption bar, the momentum trap, and all the measuring units (refer to Figure 6B). The length of the cylindrical strike bar is 300 mm, and that for the incident bar and transmitted bar is 1.5 m for both. The striker is driven by the low-pressure gun that is controlled by a control system. Different pressures can be assigned to the pressure gun, and the striker generates different incident stress waves when it hits the incident bar. Then, the wave passes the incident strain gauge and travels to the interface of the incident bar and the specimen, dividing into the transmitted wave and reflected wave, which are recorded by the strain gauges in the form of the electrical signal (in micro-voltage) that can be later converted to micro-strain by a convention coefficient K (1.54E3 for both the incident gauge and transmitted gauge). All the bars were made with 7075 aluminum alloy with Young's modulus of 70 GPa. The wave velocity in the bars was measured as 5073.8 m/s. During the test, a part of a cigarette filter of 6 mm in diameter and 7.5 mm in length was placed via vaseline as the pulse shaper at the start of the incident bar near the strike-incident interface. In addition, a high-speed camera, the Photron Fastcam SA5, was employed to record the entire fracturing process. This camera can capture images at up to 1 million frames per second. However, choosing a higher frame rate requires scarifying the brightness of the images and the number of pixels. In this paper, the frame rate was chosen as 262 500 frames per second, and the resolution was 192×96 pixels just in the zone of interest to make the best combination. The end-trigger mode was used, which means images were continuously recorded until the user pressed the trigger button at the end of the specimen's failure, with images captured before the trigger being retained in the memory.

3.3 | Experimental results

The deforming rate histories were recorded for all the specimens, and 3 distinct samples (refer to Figure 7A) are picked for numerical calibration. Different loading rates will produce different fracture toughnesses (eg, 0.46 MPa.m$^{0.5}$, 0.61 MPa.m$^{0.5}$, and 0.70 MPa.m$^{0.5}$ for Sample 1, Sample 2, and Sample 3, respectively), and their stress history curves are used to calibrate the parameters in DLSM. The history of the stress intensity factor for a typical specimen (Sample 1) is illustrated in Figure 7B. The images from the high-speed camera are also attached. In the curve, 0 μs is denoted as the moment before any movement of the incident bar. At 50 μs, the specimen underwent some deformation, but the notch did not extend. At 79 μs, a new crack was initiated at both tips of the notch. At 113 μs, the curve reached the first peak, followed by some fluctuations with other peaks. Using aluminum bars with the cigarette filter as pulse shaper, the force equilibrium was well achieved before the peak, as shown in Figure 7C. Therefore, we can use Equation 16 to estimate the dynamic stress intensity factor.

4 | PARAMETRIC STUDY

The material used in DLSM possesses the following properties: Elastic modulus E = 1.8 GPa, Poisson's ratio $\nu = 0.19$, and density $\rho = 1400$ kg/m^3, which are used to calculate the spring stiffness and motion equations. In the proposed constitutive model, 4 parameters need to be determined, ie, the ultimate spring deformation U_n^*, the ratio β, the ratio γ, and the damage-plasticity weight λ_{dp}. In the following, their influences on the initial and peak toughness, crack speed, and crack pattern are investigated. Three typical specimens, ie, Sample 1, Sample 2, and Sample 3, are used as references in the following subsections.

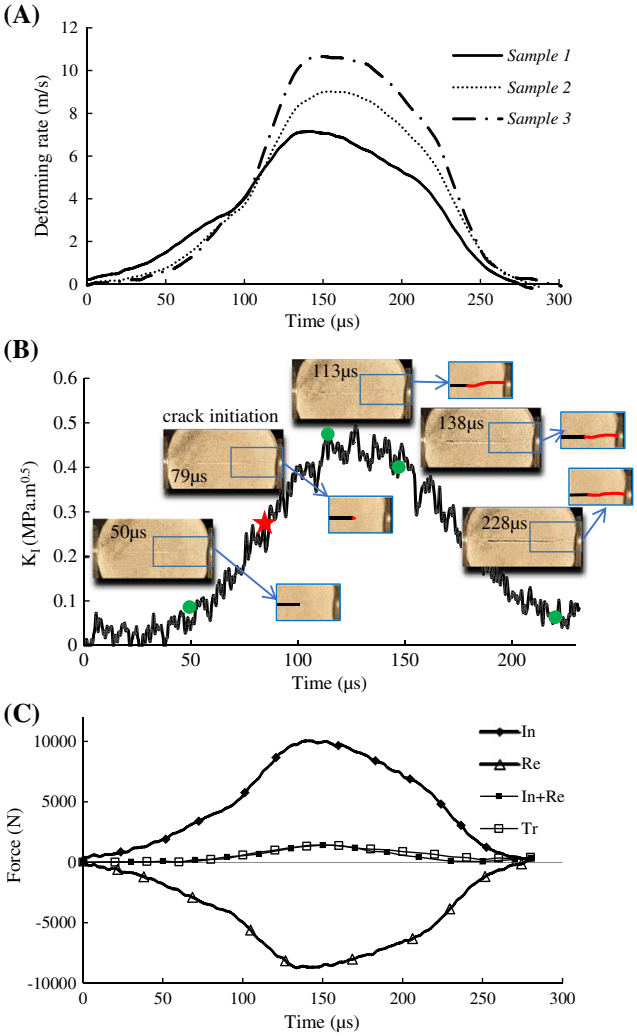

FIGURE 7 (A) Deforming rate history for 3 typical specimens. (B) History of the stress intensity factor for sample 1. (C) Dynamic force balance during the SHPB test with the CSTBD specimen; "In" and "Re" denote the forces evaluated by the incident strain wave and reflected strain wave, respectively. "In + Re" is the force acting on the specimen's interface towards the incident bar, and "Tr" is the force on the other side towards the transmission bar [Colour figure can be viewed at wileyonlinelibrary.com]

4.1 | Initial/peak toughness

To verify the effect of U_n^*, the elasto-brittle model, which is an extreme case of the proposed model when β equals 1, is employed. It is noted that, in such a constitutive model, the influences from λ_{dp} or γ do not exist. The strain rate histories in Figure 7A are used as the boundary conditions in DLSM. Figure 8A,B,C plots the relationship of U_n^* and the peak toughness with particle diameters of 0.1, 0.2, and 0.5 mm under 3 loading conditions for Sample 1, Sample 2, and Sample 3, respectively. It is noted that the increase of U_n^* causes an increase in fracture toughness, and as the particle diameter decreases, U_n^* needs to decrease as well to maintain the fracture toughness at the same level. To elaborate, the values of experimental fracture toughness are also indicated in the graphs by dashed lines. The intersects refer to the required U_n^* that can match the experimental fracture toughness, and the different intersects among the 3 diameters mean that models with D = 0.1 mm should choose lower values of U_n^* than the other two. As proper values of U_n^* need to be determined for different particle sizes, Figure 8D provides the trends and some guidance on choosing the values of U_n^*. It is noted that, in the cases of each loading rate, the change of U_n^* is approximately proportional to the variation of particle size. Therefore, a value of U_n^* for a fine particle size can be roughly estimated after 2 or 3 sets of trials based on relatively coarser sizes. This is useful when simulating extremely fine models whose simulations might take hours to complete.

The influence of λ_{dp} starts with unloading and reloading in the constitutive model. In other words, the influence is supposed to occur after crack initiation. Thus, there should be no difference at the initial toughness, while it will change the history path from the initial to the peak toughness. In the following numerical simulations, the values of β, γ, *and*

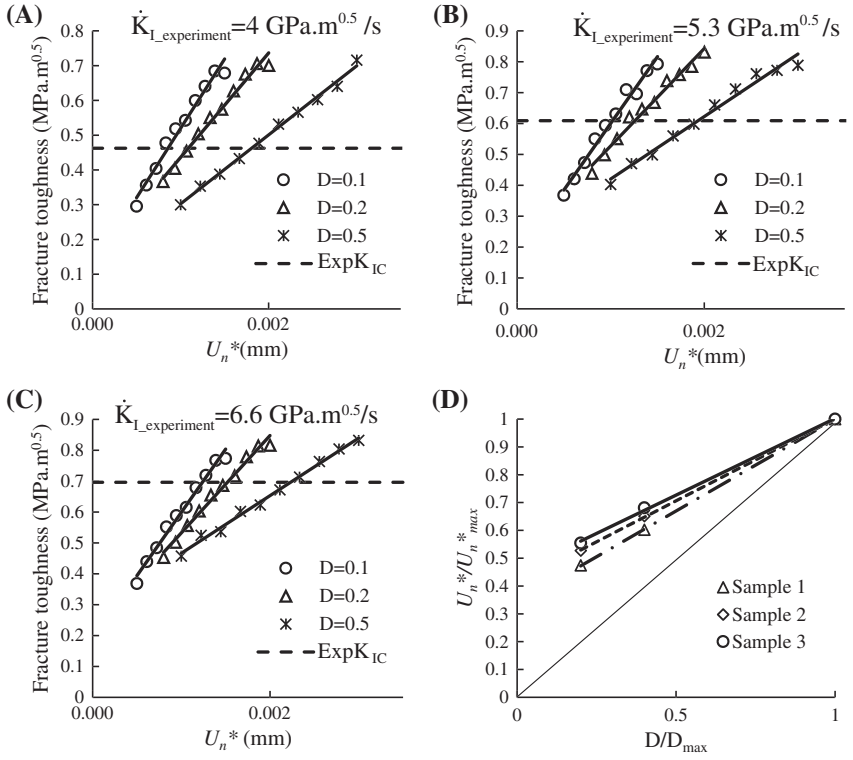

FIGURE 8 The relationship between the fracture toughness and value of *Un** with different particle sizes in for 3 different loading rates. (A) Sample 1 with 4.0 GPa.m0.5/s. (B) Sample 2 with 5.3 GPa.m0.5/s. (C) Sample 3 with 6.6 GPa.m0.5/s. (D) The relationship of the selected particle sizes and values of the trend of *Un**

U_n* are kept constant, and the influences from different λ_{dp} values are investigated. However, from the historical curves for the various λ_{dp} values illustrated in Figure 9A, nearly no change is observed for the duration from crack initiation to peak, although the post-peak curves look different. Table 2 lists the peak time and peak stress for different λ_{dp}, and it is noted that their time to peak and the associated peak stress are almost the same. Therefore, it is concluded that the influence of λ_{dp} on initial toughness is zero and on peak toughness is minimal.

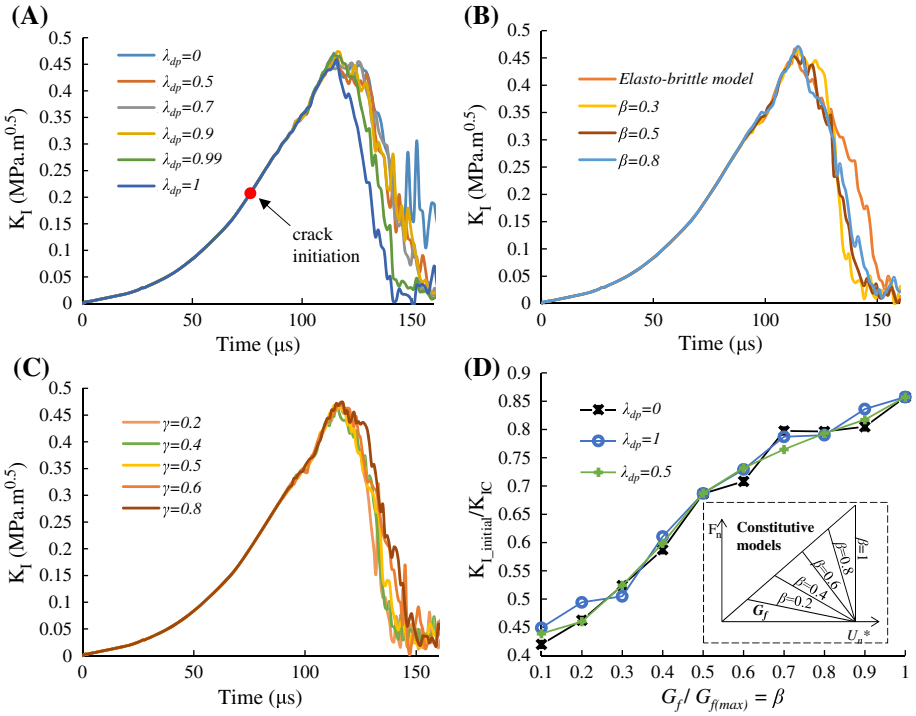

FIGURE 9 History of the stress intensity factor (A) with different λdp; $\beta = 0.3$ and $\gamma = 0.5$, (B) with different β; $\gamma = 0.5$, $\lambda dp = 1$, and (C) with different γ; $\beta = 0.5$, $\lambda dp = 1$. (D) The ratio of the stress intensity at the initiation and peak with change of the fracture energy *Gf* [Colour figure can be viewed at wileyonlinelibrary.com]

TABLE 2 Peak time and peak stress for different plastic damage models

λ_{dp}	Peak Time, μs	Peak Stress, kPa
0	114.5	115.3
0.5	115.8	113.5
0.7	113.1	111.3
0.9	114.5	116
0.99	115.8	114.6
1	115.8	112.2

When setting $\gamma = 0.5$, a smaller β in the constitutive model means a gentler slope for the tensile force drop in the normal spring. The different bilinear cohesive models are tested, and the results are plotted in Figure 9B. Additionally, the normal force can drop with 2 slopes by adjusting γ into a trilinear form, and the results are plotted in Figure 9C. From Figure 9A,B,C, it is realized that changes of λ_{dp}, β and γ all can generate the curves fitting the same peak toughness, so it might be easier for calibration in this dynamic fracturing problems for CSTBD if removing some parameters in the proposed constitutive model.

For dynamic fracture tests in CSTBD specimens, the initial toughness (corresponding to the crack initiation) differs from the peak toughness, which is affirmed in the numerical and experimental results. When fixing the base of the triangle for the micro-constitutive model as depicted in Figure 9D, the ratio of initial and peak toughness is related to the fracture energy (G_f), which is the area under the curve of constitutive model. For illustration, U_n^* is set to a constant, $\gamma = 0.5$, and increasing β will increase G_f (refer to Figure 9D), which causes the fracture toughness to increase as well. However, the degrees of change in initial and peak toughness are not identical. The ratio of initial and peak toughness increases with increased G_f, and the influences from λ_{dp} are negligible, as observed in Figure 9D.

4.2 | Crack speed

According to the elastic wave theory,[28] the Rayleigh surface wave velocity, which is regarded as the limit of the cracking velocity in the solids, is 668.3 m/s for our 3D printed specimens. In real materials, experiments show that the crack velocities are always smaller than the Rayleigh wave speed due to material or crack path imperfection.[29,30] In our experiment, the actual crack speed failed to be obtained by visually tracking the crack tips. Because the average size of the powder is too small, as shown in Figure 6A, the crack opening at the tip was tiny, and our high-speed camera did not have enough pixels to monitor the crack tip in the entire process. Thus, the crack initiation point marked in Figure 7 B was chosen by our observation of any cracks extending from the tips. It might be true that the actual crack tips are far from what we observed. If we assume correctly that the cracks reached the edges of the loading boundary simultaneously at the peak load, the crack speed in the 3D printed specimens is approximately 242.6 m/s, which is 36% of the Rayleigh wave speed.

Many tests are conducted for different particle sizes on the elasto-brittle models, the results of which are shown in Figure 10A. It seems that U_n^* causes negligible declination in crack speed. It is also noted that the experimental crack speed can hardly be simulated by the elasto-brittle model. Therefore, the cohesive models are tried in bilinear forms whose shapes are governed by β. The size effect on the crack speed is also investigated with particle sizes of 0.1, 0.2, and 0.5 mm. The results plotted in Figure 10B indicate: (1) that the parameter β can vary the crack speed (eg, from approximately 0.2 V_R to 0.6 V_R in our simulation) and (2) that the smaller particle size generates a higher crack speed.

Setting λ_{dp} to 1 and keeping the maximum micro tensile strength F_n^* fixed (ie, keeping βU_n^* constant), the crack speed is calculated with different combinations of β and γ. The results of crack speed are plotted in Figure 10C. It is noted that both β and γ can change the crack speed, but the influence of β is larger than that of γ. In addition, negligible influence from U_n^* is observed in the cohesive models when using different values of βU_n^* and γ is set to 0.5. Lastly, the crack speed with 3 values of λ_{dp} are presented in Figure 10D, which shows that the crack speed is mainly governed by β with little influence of λ_{dp} observed.

The actual crack speed in the physical tests may be reduced due to material imperfection. Therefore, the material heterogeneity is incorporated in our models to mimic the feature. A 2-phase model is created with random distribution of either spheres or Voronoi diagrams. The base material is grayish, and the second material is greenish, as seen in Figure 11. The ultimate normal deformations are denoted as $U_n^*(1)$ and $U_n^*(2)$, respectively. In the random spherical

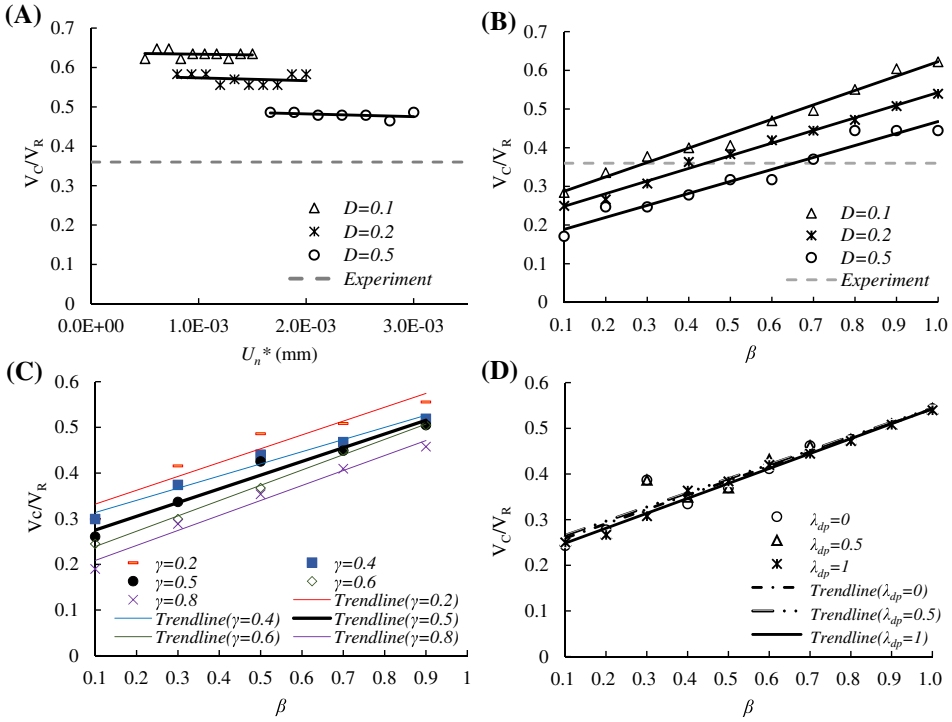

FIGURE 10 (A) The crack velocity in the elasto-brittle model; $\beta = 1$. (B) Crack speed with change of β for different particle sizes; $\gamma = 0.5$, $\lambda dp = 1$. (C) Crack speed with different β and γ; $\lambda dp = 1$ (D) Crack speed with 3 λdp values; $\gamma = 0.5$ [Colour figure can be viewed at wileyonlinelibrary.com]

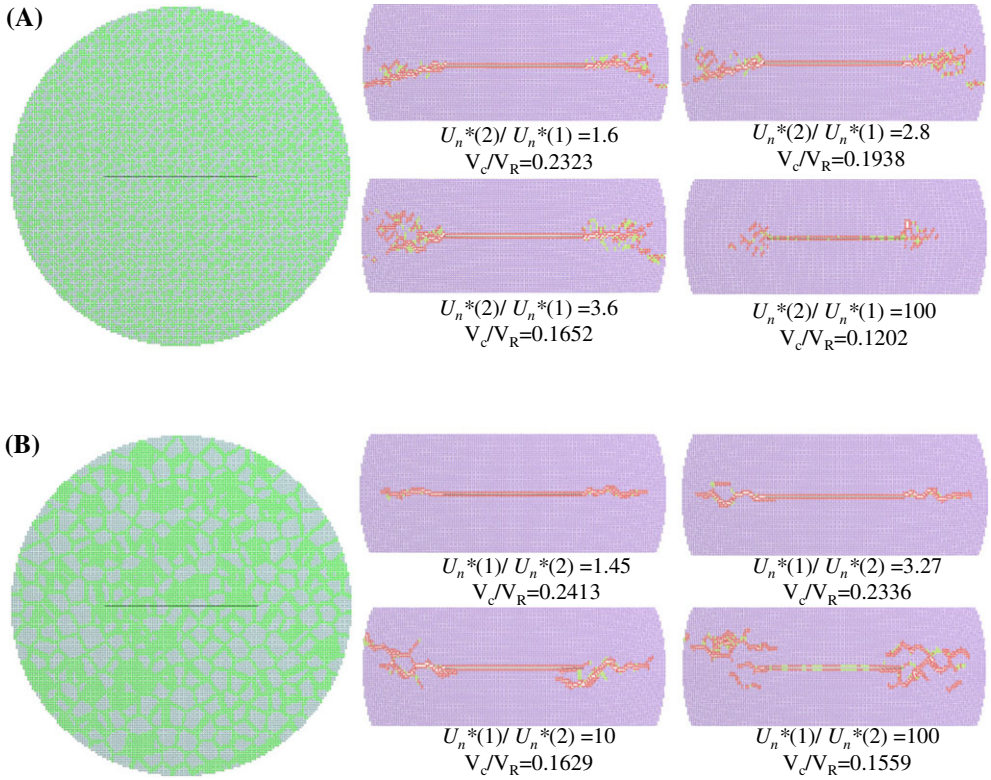

FIGURE 11 The influence of material heterogeneity on crack path and crack velocity. (A) Random spherical 2-phase model. (B) Two-phase model in Voronoi diagram. The base material is denoted as the material with *Un**(1) and the greenish material is with *Un**(2) [Colour figure can be viewed at wileyonlinelibrary.com]

2-phase model, the base material is weaker than the second material. It is observed in Figure 11A that the crack path becomes more dispersed as the ratio of the ultimate deformation is increased. When the ratio becomes extremely large, the crack is discontinuous and very difficult to extend. Moreover, the crack speed decreases as the ratio of the ultimate deformation increases. It is mentioned that the crack speed in the homogeneous model with this constitutive model is 0.32 V_R. In the 2-phase model in the Voronoi diagram, the base material is stronger than the second material. The crack path is mainly along the second material. Similarly, the crack becomes more dispersed and discontinuous when the ratio becomes larger, and the crack speed decreases. Therefore, it is realized that the degree of material heterogeneity obviously affects the crack pattern and the associated crack speed, which must be accounted for in physical tests on rocks.

4.3 | Crack patterns

It needs to be mentioned that the load drop in DLSM is more rapid than in the experiment. For example, the force drops to zero at approximately 150 μs in Figure 9A,B,C, while that in the experiment is later than 200 μs in Figure 7B. By changing the different parameters, we do not find any solution that reduces the slope of the load drop, so some crack patterns are selected for investigation. In the cases of different λ_{dp} in Figure 12A,B,C, the crack initiations occur at the same moment (76.8 μs) with the same initial toughness (0.20 MPa.$m^{0.5}$). The crack path becomes dispersed as it approaches the boundary. After the peak time (approximately 115 μs), crack zones of significant size formed, which caused the rapid load drop in the macro behavior. To compare, after 115 μs in the experiment, the crack path just became clearer as the crack width was wider, but the crack remained straight, and no secondary cracks were observed. Therefore, one can deduce that the sudden load drop with a disperse crack pattern is the result of the lattice structure. This regular lattice alignment probably limits the smooth extension of the line crack near the loading boundaries. The dispersion of the crack causes further stress concentration in that area, and the sudden release of the fracture energy causes the sudden load drop in the curve. The crack dispersion may be from particle packaging instability near the boundaries. Densely packed particles with random diameters may improve the post-peak behavior, but this is out of the scope of the paper and will not be addressed.

Among the cases of different λ_{dp} in Figure 12A,B,C, it is observed that all the cracks propagate horizontally with minor initial differences. However, even though the differences are small, they accumulate and result in a noticeable difference at the moment of peak stress. At 129.3 μs, which is in the post-peak period, different areas of fractured zones are formed. It reveals that the influence from λ_{dp} is not reflected on the K_I history curve but on the crack patterns.

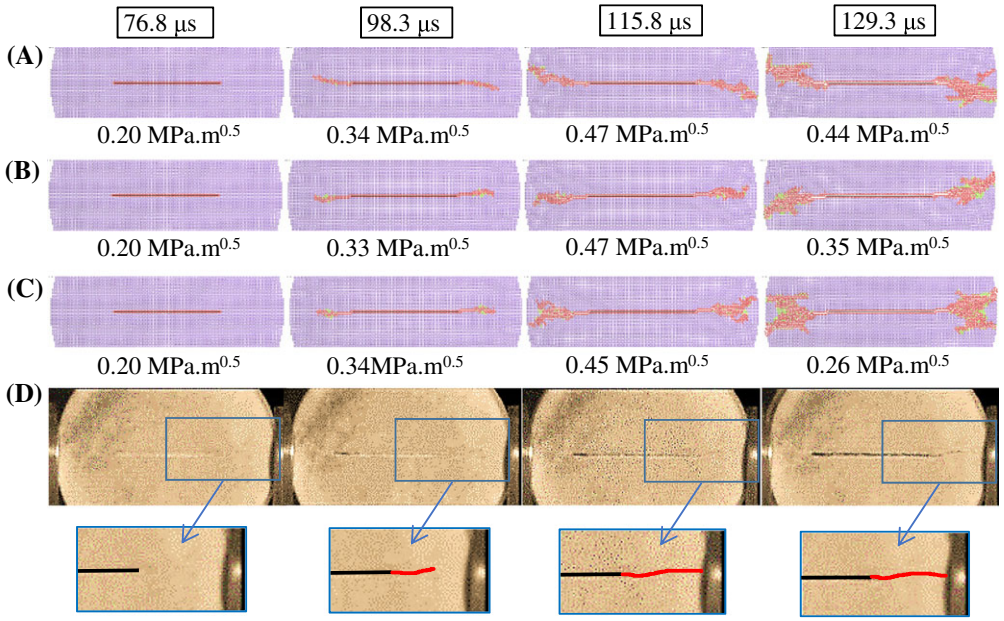

FIGURE 12 Comparisons of the crack patterns among the constitutive models with different values of λdp: (A) $\lambda dp = 0$ (B) $\lambda dp = 0.99$ (C) $\lambda dp = 1$ (D) experiment. The third column is the time (115.8 μs) near peak load [Colour figure can be viewed at wileyonlinelibrary.com]

4.4 | Simplified constitutive model

The proposed constitutive model is simple but considers many aspects in the simulation cases. However, for our dynamic CSTBD simulations, the full model can be further simplified. In the original proposed constitutive model, 4 parameters need to be determined: β, U_n^*, λ_{dp}, and γ. Without considering the time in the simulation, the crack patterns generated are similar among the combinations of the parameters and well matched to the experiment before the peak toughness. Indeed, the crack pattern associated with time (eg, the crack initiation moment and peak moment) is influenced by the fracture toughness and crack speed. From the parametric study, the relationships between the parameters and the fracture toughness and crack speed are summarized in Table 3. It is shown that β has influences on both fracture toughness and crack speed and that U_n^* mainly affects the fracture toughness rather than the crack speed. λ_{dp} has minimal influence on either fracture toughness or crack speed, and γ has influence on both. However, γ's degree of influence is less than U_n^*'s on fracture toughness and less than β's on the crack speed. Therefore, for simplicity, the value of γ can be fixed at 0.5 so that the original constitutive model can be simplified to a bilinear model. It is noted that the bilinear model is also more computationally efficient than the trilinear model. Because λ_{dp} does not affect the crack behavior much, it can be set to a constant (eg, $\lambda_{dp} = 1$ for a pure damage model). Therefore, the simplified constitutive model is formed as a special case of the proposed model as plotted in Figure 2D. The normal force F_n can be expressed as

$$F_n = (1-D_n)k_nU_n \tag{17}$$

where k_n is the initial normal spring stiffness and D_n is the dimensional damage stiffness coefficient:

$$D_n = \begin{cases} 0 & ; \quad u_n^h \le \beta U_n^* \\ 1 & ; \quad u_n^h \ge U_n^* \\ \left(\frac{1}{1-\beta}\right)\left(1-\frac{\beta U_n^*}{u_n^h}\right) & ; \quad else \end{cases}. \tag{18}$$

At this stage, there are only 2 parameters (ie, β and U_n^*) to be determined. The crack speed is mainly governed by β, and the fracture toughness is produced by the combination of β and U_n^*. To find the combinations that produce the same level

TABLE 3 Influential factors on fracture toughness and crack speed in the proposed constitutive model

	Fracture Toughness	Crack Speed
β	Yes	Yes
U_n^*	Yes	Minimal
λ_{dp}	Minimal	Minimal
γ	Yes (less than U_n^*)	Yes (less than β)

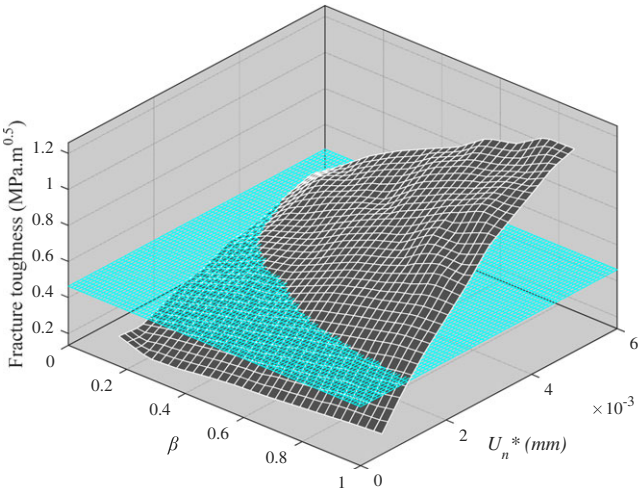

FIGURE 13 An example of the profile on fracture toughness with combinations of Un^* and β. The particle size in DLSM is 0.2 mm and it is simulating Sample 1 [Colour figure can be viewed at wileyonlinelibrary.com]

of peak fracture toughness, profiles of fracture toughness are generated. Referring to the example shown in Figure 13, the plane representing the value of the experimental fracture toughness cuts into the profile and helps to project the intersection onto a curve on the β-U_n^* plane. Three different particle sizes (ie, 0.1, 0.2, 0.5 mm) are used, and the projected curves

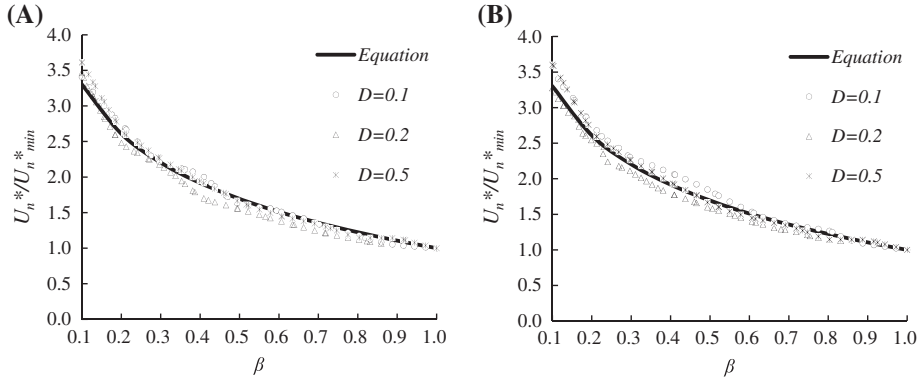

FIGURE 14 Normalized projected line from the profile of simulating (A) Sample 1 (B) Sample 3

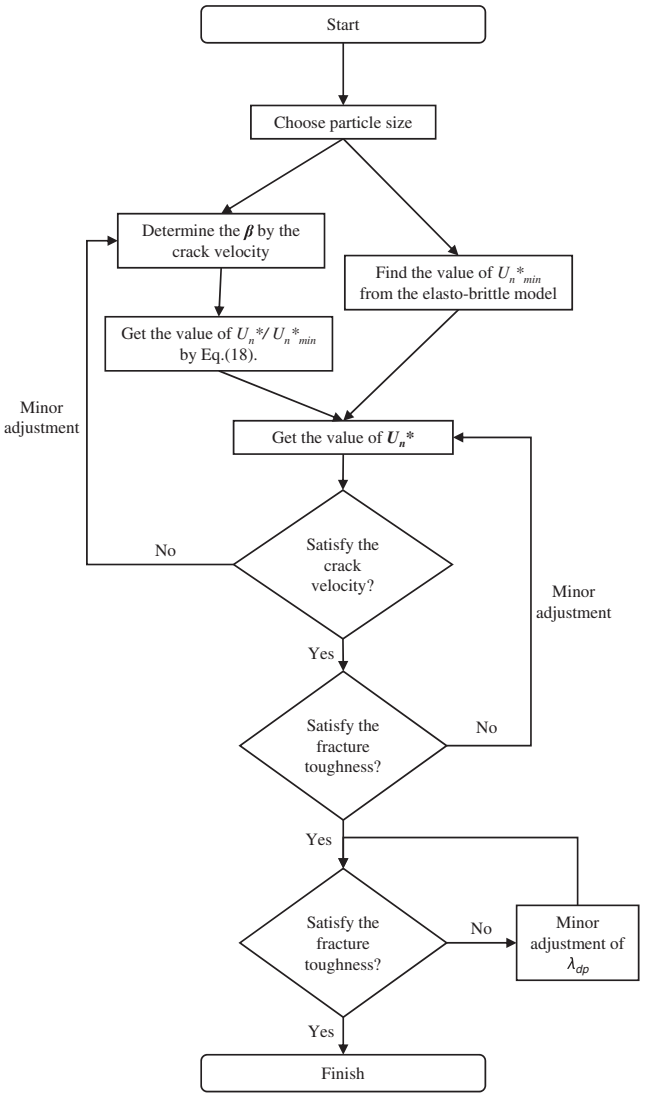

FIGURE 15 Flow chart of the procedures on parameter selection

are normalized on the Y-axis by $U_n^*/U_n^*_{min}$, which is illustrated in Figure 14. $U_n^*_{min}$ is the minimum value of the critical normal spring deformation and equals that in the elasto-brittle constitutive model (ie, $\beta = 1$). It is noted that all the projected curves squeeze to a uniform curve after normalization, although the simulations are carried out at different loading rates (ie, on Sample 1 and Sample 3 in Figure 14). A uniform equation is proposed to fit the shape of the curve for different particle sizes and loading rates, which is

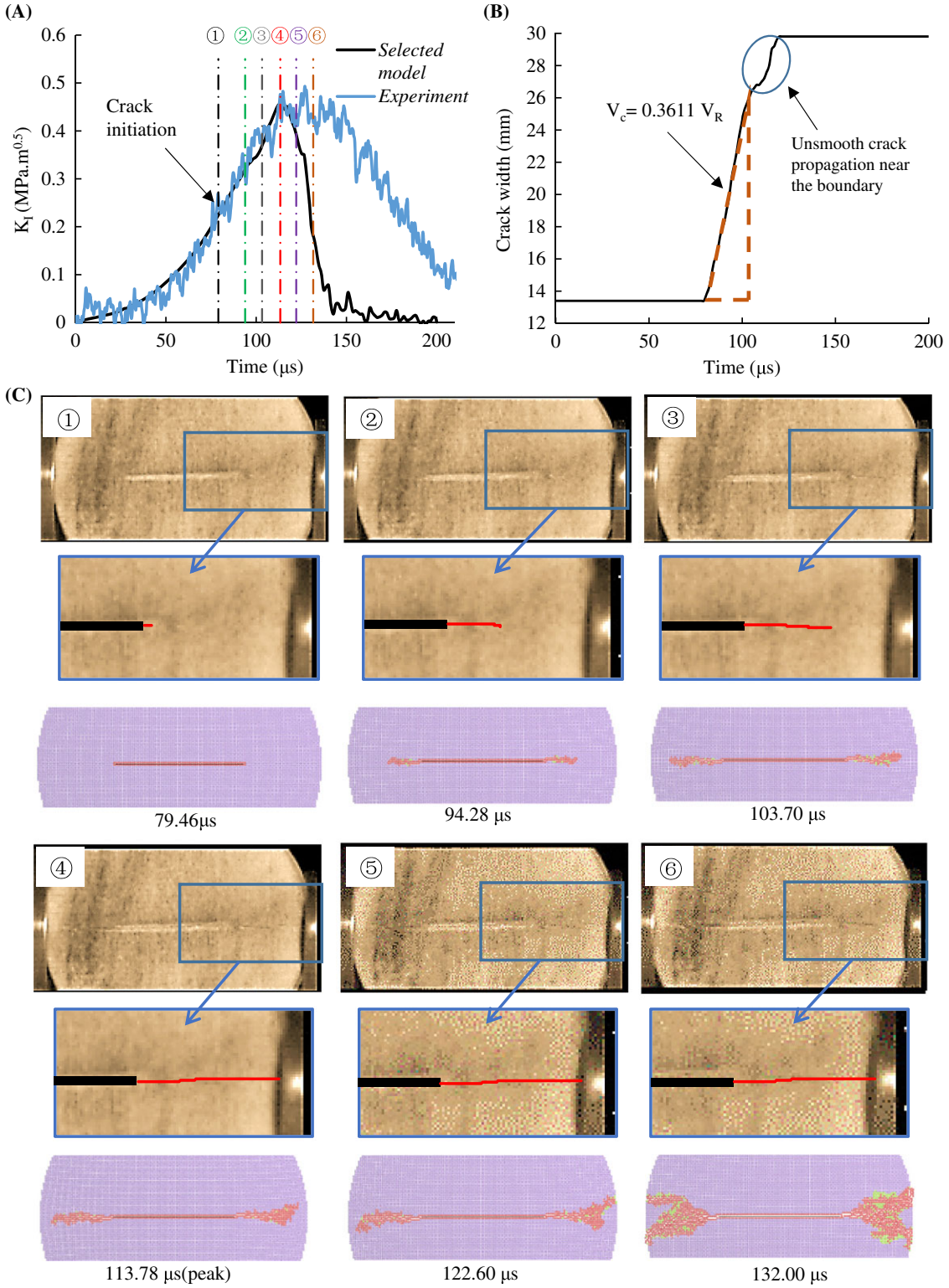

FIGURE 16 (A) History of stress intensity factor from the selected model and experiment. (B) The curve of crack width versus time. (C) The development of the crack path in the experiment and in DLSM with the selected parameters [Colour figure can be viewed at wileyonlinelibrary.com]

$$\frac{U_n^*}{U_{n\_\min}^*} = -\ln(\beta) + 1. \tag{19}$$

By Equation 19, the ultimate normal spring deformation can be estimated at different β once DLSM is calibrated with that in the elasto-brittle constitutive model.

4.5 | Parameter selection

In this section, we summarize the procedures for parameter selection with a flow chart in Figure 15. The appropriate particle size is first chosen based on the size of the model and the computational ability. Then, β is determined according to the crack velocity. Via Equation 19, the ratio of $U_n^*/\ U_n^*{}_{min}$ can be identified, while the value of $U_n^*{}_{min}$ is obtained from the elasto-brittle model through trial and error. Lastly, the first estimation of U_n^* is back-calculated. After this stage, some examinations will be carried out. If the simulation does not satisfy the crack speed, minor adjustment of the value of β is needed, followed by calculation of a new U_n^*. If the simulation does not satisfy the fracture toughness, minor adjustment of the value of U_n^* is needed. If the simulation satisfies both the crack speed and fracture toughness but not the crack pattern, a change of the value of λ_{dp} may help.

To illustrate, the parameters for Sample 1 are presented. First, we choose the particle size of 0.2 mm. Second, as the crack velocity obtained from the experiment is 0.36 V_R, we can determine the value of β to be 0.45 according to Figure 10 B. Third, the value of $U_n^*/\ U_n^*{}_{min}$ is 1.799 by Equation 19. Fourth, the value of U_n^* in the elasto-brittle model is found to be 1.112E − 3 mm, which is regarded as $U_n^*{}_{min}$. Lastly, the value of U_n^* is back-calculated to be 2E − 3 mm. To conclude, the values for the parameters are $\beta = 0.45$, $U_n^* = 0.002$ mm, $\lambda_{dp} = 1$, and $\gamma = 0.5$.

The match of the fracture toughness to the experiment is shown in Figure 16A. It is noted that Equation 19 works well in this case because the peak of the selected model matches that in the experiment. The graph for the crack extension is drawn in Figure 16B, where the crack velocity is taken in the linear part of the curve with a crack speed ratio of 0.3611. It is close to our target of 0.36, so no adjustment of β is needed. Additionally, as the fracture toughness is well simulated, the value of U_n^* does not need to be adjusted either. The crack patterns are shown in Figure 16C. The different corresponding times of the figures are also marked in Figure 16A. The crack propagates from the crack tips to the loading edges in a relatively straight line, which is similar to the experiment. However, at the peak time, the crack tips are dispersed rather than propagating horizontally such that the crack patterns differ from the experiment, and the reason has been discussed in Section 4.3. To conclude, the selected constitutive model has successfully simulated the experimental fracture toughness, crack speed, and crack patterns before the peak.

When the same set of parameters for Sample 1 (ie, β, U_n^*, λ_{dp}) are used for simulations of Sample 2 and Sample 3, the influences of loading rate dependency on fracture toughness and crack speed are observed, as depicted in Figure 17, although we have not incorporated the rate-dependent parameters into the micro-constitutive model. Zhao et al[21] noted that the micro-structure of the model contributes to the rate dependency. However, the scope of this paper is prediction of the property of crack propagation by a constitutive model under a fixed loading rate. The parameters need to be adjusted to fully match the experiment for Sample 2 and Sample 3, which is a deficiency of the model when not considering the rate dependency in the constitutive equations. Thus, at least 3 parameters must be determined: the calibration of U_n^* is necessary; the value of β can be estimated by crack speed; and the calibration of λ_{dp} is optional.

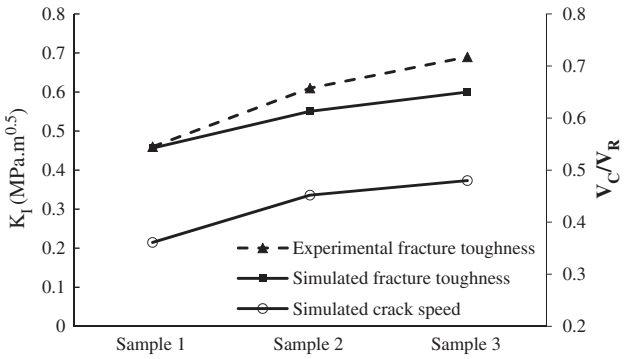

FIGURE 17 Simulated fracture toughness and crack speed using the calibrated parameters for Sample 1

5 | CONCLUSION

In this paper, a damage-plasticity model was developed and implemented into a 2D DLSM, which is used to study the dynamic crack propagation with the help of a 3D printing technique. The damage-plasticity DLSM was first verified against analytical elastic solutions within the elastic region of the constitutive model. In addition, 2 examples of dynamic crack propagation on wing cracks in resin and crack coalescence on a perforated epoxy plate were simulated, and the results agreed well with the experiment from the literature. Then, an experiment in the SHPB system on crack propagation with 3D printed specimens was carried out as a benchmark for numerical simulation. Both the stress/strain history and crack patterns from a high-speed camera were recorded. The specimens showed brittle fracturing behaviors under various loading rates, and the stress equilibrium was successfully achieved using the aluminum bars and cigarette filters as pulse shapers. With the experimental results, a comprehensive parametric study was conducted to account for the fracture toughness, crack speed, and crack pattern. It is realized that λ_{dp} only has influence on the crack patterns and that U_n^* affects the fracture toughness to a large extent. Both β and γ have an influence on the fracture toughness and crack velocity, but the degree of influence of γ is less pronounced than that of β. Moreover, the influences from the particle size and material heterogeneity were also incorporated. After the parametric study, a simplified version of the constitutive model was proposed. The selection of the values of the parameter was demonstrated as an instructive case in the experiment, with the features of the crack propagation successfully simulated.

However, the current constitutive model is only applicable to prediction of the crack behavior under a fixed loading rate. This shortcoming is due to the lack of full consideration of the rate dependency in the constitutive equations, especially the micro-structural characteristics, which need further study in the future.

ORCID

Chao Jiang http://orcid.org/0000-0002-6069-5196
Gao-Feng Zhao http://orcid.org/0000-0001-9962-8743

REFERENCES

1. Lee H, Jeon S. An experimental and numerical study of fracture coalescence in pre-cracked specimens under uniaxial compression. *Int J Solids Struct*. 2011;48(6):979-999. https://doi.org/10.1016/j.ijsolstr.2010.12.001
2. Haeri H, Shahriar K, Marji MF, Moarefvand P. Experimental and numerical study of crack propagation and coalescence in pre-cracked rock-like disks. *Int J Rock Mech Min Sci*. 2014;67:20-28. https://doi.org/10.1016/j.ijrmms.2014.01.008
3. Haeri H, Khaloo A, Marji MF. Experimental and numerical analysis of Brazilian discs with multiple parallel cracks. *Arab J Geosci*. 2015;8(8):5897-5908. https://doi.org/10.1007/s12517-014-1598-1
4. Dai S, Augarde C, Du C, Chen D. A fully automatic polygon scaled boundary finite element method for modelling crack propagation. *Eng Fract Mech*. 2015;133:163-178. https://doi.org/10.1016/j.engfracmech.2014.11.011
5. Ayatollahi MR, Aliha MRM, Hassani MM. Mixed mode brittle fracture in PMMA—an experimental study using SCB specimens. *Mater Sci Eng A*. 2006;417(1-2):348-356. https://doi.org/10.1016/j.msea.2005.11.002
6. Landis CM, Pardoen T, Hutchinson JW. Crack velocity dependent toughness in rate dependent materials. *Mech Mater*. 2000;32(11):663-678. https://doi.org/10.1016/S0167-6636(00)00031-4
7. Zhang QB, Zhao J. Quasi-static and dynamic fracture behaviour of rock materials: phenomena and mechanisms. *Int J Fract*. 2014;189(1):1-32. https://doi.org/10.1007/s10704-014-9959-z
8. Bhat HS, Rosakis AJ, Sammis CG. A micromechanics based constitutive model for brittle failure at high strain rates. *J Appl Mech*. 2012;79(3):031016-031016. https://doi.org/10.1115/1.4005897
9. Jing L, Hudson JA. Numerical methods in rock mechanics. *Int J Rock Mech Min Sci*. 2002;39(4):409-427. https://doi.org/10.1016/S1365-1609(02)00065-5
10. Cundall P.A. A computer model for simulating progressive, large-scale movements in blocky rock systems. in *Proceedings of the international symposium on rock fracture*. 1971. Nancy: International Society for Rock Mechanics (ISRM).
11. Zhao G-F. Development of micro-macro continuum-discontinuum coupled numerical method. 2010. *École Polytechnique Fédérale de Lausanne*.
12. Zhao G-F, Fang JN, Zhao J. A 3D distinct lattice spring model for elasticity and dynamic failure. *Int J Numer Anal Methods Geomech*. 2011;35(8):859-885. https://doi.org/10.1002/nag.930

13. Zhu JB, Zhao GF, Zhao XB, Zhao J. Validation study of the distinct lattice spring model (DLSM) on P-wave propagation across multiple parallel joints. *Comput Geotech*. 2011;38(2):298-304. https://doi.org/10.1016/j.compgeo.2010.12.002
14. Zhao G-F. Modelling 3D jointed rock masses using a lattice spring model. *Int J Rock Mech Min Sci*. 2015;78:79-90. https://doi.org/10.1016/j.ijrmms.2015.05.011
15. Kazerani T, Zhao GF, Zhao J. Dynamic fracturing simulation of brittle material using the distinct lattice spring method with a full rate-dependent cohesive law. *Rock Mech Rock Eng*. 2010;43(6):717-726. https://doi.org/10.1007/s00603-010-0099-0
16. Zhao G-F, Kazerani T, Man K, Gao M, Zhao J. Numerical study of the semi-circular bend dynamic fracture toughness test using discrete element models. *Sci China Technol Sci*. 2015;58(9):1587-1595. https://doi.org/10.1007/s11431-015-5887-z
17. Gui Y, Zhao GF. Modelling of laboratory soil desiccation cracking using DLSM with a two-phase bond model. *Comput Geotech*. 2015;69:578-587. https://doi.org/10.1016/j.compgeo.2015.07.001
18. Zhao G-F, Khalili N. Graphics processing unit based parallelization of the distinct lattice spring model. *Comput Geotech*. 2012;42:109-117. https://doi.org/10.1016/j.compgeo.2012.01.004
19. Zhao G-F, Fang J, Zhao J. A MLS-based lattice spring model for simulating elasticity of materials. *Int J Comput Methods*. 2012;9: https://doi.org/10.1142/S0219876212500375(03):1250037
20. Zhao G-F. Development of the distinct lattice spring model for large deformation analyses. *Int J Numer Anal Methods Geomech*. 2014;38(10):1078-1100. https://doi.org/10.1002/Nag.2249
21. Zhao G-F, Russell AR, Zhao X, Khalili N. Strain rate dependency of uniaxial tensile strength in Gosford sandstone by the distinct lattice spring model with X-ray micro CT. *Int J Solids Struct*. 2014;51(7-8):1587-1600. https://doi.org/10.1016/j.ijsolstr.2014.01.012
22. Gercek H. Poisson's ratio values for rocks. *Int J Rock Mech Min Sci*. 2007;44(1):1-13. https://doi.org/10.1016/j.ijrmms.2006.04.011
23. Nemat-Nasser S, Horii H. Compression-induced nonplanar crack extension with application to splitting, exfoliation, and rockburst. *J Geophys Res Solid Earth*. 1982;87(B8):6805-6821. https://doi.org/10.1029/JB087iB08p06805
24. Wang Y, Mora P. Modeling wing crack extension: implications for the ingredients of discrete element model. *Pure Appl Geophys*. 2008;165(3-4):609-620. https://doi.org/10.1007/s00024-008-0315-y
25. Al-Ostaz A, Jasiuk I. Crack initiation and propagation in materials with randomly distributed holes. *Eng Fract Mech*. 1997;58(5-6):395-420. https://doi.org/10.1016/S0013-7944(97)00039-8
26. Jiang C, Zhao G-F, Zhu J, Zhao Y-X, Shen L. Investigation of dynamic crack coalescence using a gypsum-like 3d printing material. *Rock Mech Rock Eng*. 2016;49(10):3983-3998. https://doi.org/10.1007/s00603-016-0967-3
27. Zhang S, Wang Q-Z. Determination of rock fracture toughness by split test using five types of disc specimens. *Rock Soil Mech*. 2009;30:12-18.
28. Foti S. Multistation methods for geotechnical characterization using surface waves. 2000. *Politecnico di Torino*.
29. Fineberg J, Gross SP, Marder M, Swinney HL. Instability in dynamic fracture. *Phys Rev Lett*. 1991;67(4):457-460.
30. Ravi-Chandar K. Dynamic fracture of nominally brittle materials. *Int J Fract*. 1998;90(1/2):83-102. https://doi.org/10.1023/a:1007432017290

How to cite this article: Jiang C, Zhao G-F. Implementation of a coupled plastic damage distinct lattice spring model for dynamic crack propagation in geomaterials. *Int J Numer Anal Methods Geomech*. 2018;42:674–693. https://doi.org/10.1002/nag.2761